

www.acsami.org Research Article

# Self-Assembled Complex Three-Phase Core—Shell Nanostructure of Au—CoFe<sub>2</sub>—TiN with a Magneto-Optical Coupling Effect

Jiawei Song, Di Zhang, Ping Lu, Yizhi Zhang, Haohan Wang, Hongyi Dou, Xiaoshan Xu, Julia Deitz, Xinghang Zhang, and Haiyan Wang\*



Cite This: ACS Appl. Mater. Interfaces 2023, 15, 37810–37817



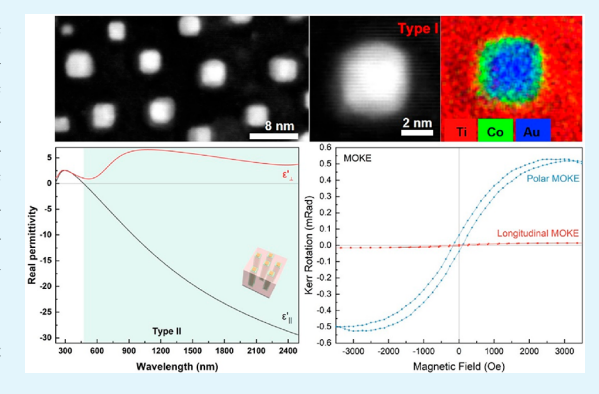
**ACCESS** I

III Metrics & More

Article Recommendations

s Supporting Information

ABSTRACT: Nanostructured plasmonic—magnetic metamaterials have gained great research interest due to their enhanced magneto-optical coupling effects. Here, we report a complex three-phase nanocomposite design combining ferromagnetic CoFe<sub>2</sub> with plasmonic TiN and Au as a multifunctional hybrid metamaterial using either a cogrowth or a templated method. Via the first method of cogrowing three phases, three different morphologies of Au–CoFe<sub>2</sub> core–shell nanopillars were formed in the TiN matrix. Via the second method of sequential deposition of a TiN–Au seed layer and a TiN–CoFe<sub>2</sub> layer, highly ordered and uniform single-type core—shell nanopillars (i.e., the CoFe<sub>2</sub> shell with a Au core) form in the TiN matrix. Both cogrowth and templated growth TiN–CoFe<sub>2</sub>–Au hybrid systems exhibit excellent epitaxial quality, hyperbolic dispersion, magnetic anisotropy, and a magneto-optical coupling effect.



This study provides an effective approach for achieving highly uniform multiphase vertically aligned nanocomposite structures with well-integrated optical, magnetic, and coupling properties.

KEYWORDS: vertically aligned nanocomposites, core—shell nanopillars, hyperbolic dispersion, magnetic anisotropy, magneto-optical coupling

#### INTRODUCTION

Magnetic storage technology relies on the control of the magnetization response to external stimuli. Magnetic storage devices nowadays seek high storage density, fast switching speed, and low power consumption.<sup>2</sup> As an example, perpendicular magnetic anisotropy materials are widely used in spintronic memory devices due to their higher storage density than longitudinal magnetic materials.<sup>3</sup> Most reported magnetic storage applications rely on electrical-control of the magnetization, such as field-induced switching<sup>4</sup> or currentinduced spin-orbit torques. However, those electrical switching methods require a continuous external magnetic field, limiting their applications in nonvolatile memory storage. Magneto-optical (MO) metamaterials have recently attracted much attention due to their ability to correlate the optical response with magnetic spins through a magneto-optical (MO) coupling effect.<sup>6</sup> In this way, the magnetization switching can be realized without continuously applying an external magnetic field. The MO coupling effects can be potentially used as optical modulators and switches, sensitive magnetization detectors, and for MO data storage.6-12

Magneto-optic properties have been studied in various material designs, such as 1D grating of ferromagnetic metals (i.e., Co, Ni, and  $Fe^{13,14}$ ), multilayers of plasmonic/magnetic materials (i.e.,  $Au/Co^{15}$ ), and nanostructured plasmonic/

magnetic composites (i.e., core—shell nanoparticles 16,17). Compared to the pure ferromagnetic design, combining plasmonic materials with ferromagnetic materials offers a great opportunity to enhance the MO interaction due to their ability to confine light into a subwavelength scale. 6,8 Considering the high optical loss of plasmonic metals, incorporating low-loss plasmonic materials in plasmonic/magnetic metamaterials opens interesting perspectives in enhancing the MO response. Transition-metal nitrides (e.g., TiN, ZrN, and HfN) are good candidates for low-loss plasmonic materials because of their similar optical response to noble metals and their superior structural stability and durability. 18–21

The hybrid nanostructured metamaterial could be achieved by various methods, such as lithography, multistep deposition, and anodic alumina oxide template growth. <sup>22–24</sup> Recently, onestep self-assembled vertically aligned nanocomposites (VANs) offer a cost-effective alternative to fabricate hybrid metamate-

Received: May 11, 2023 Accepted: July 11, 2023 Published: July 26, 2023





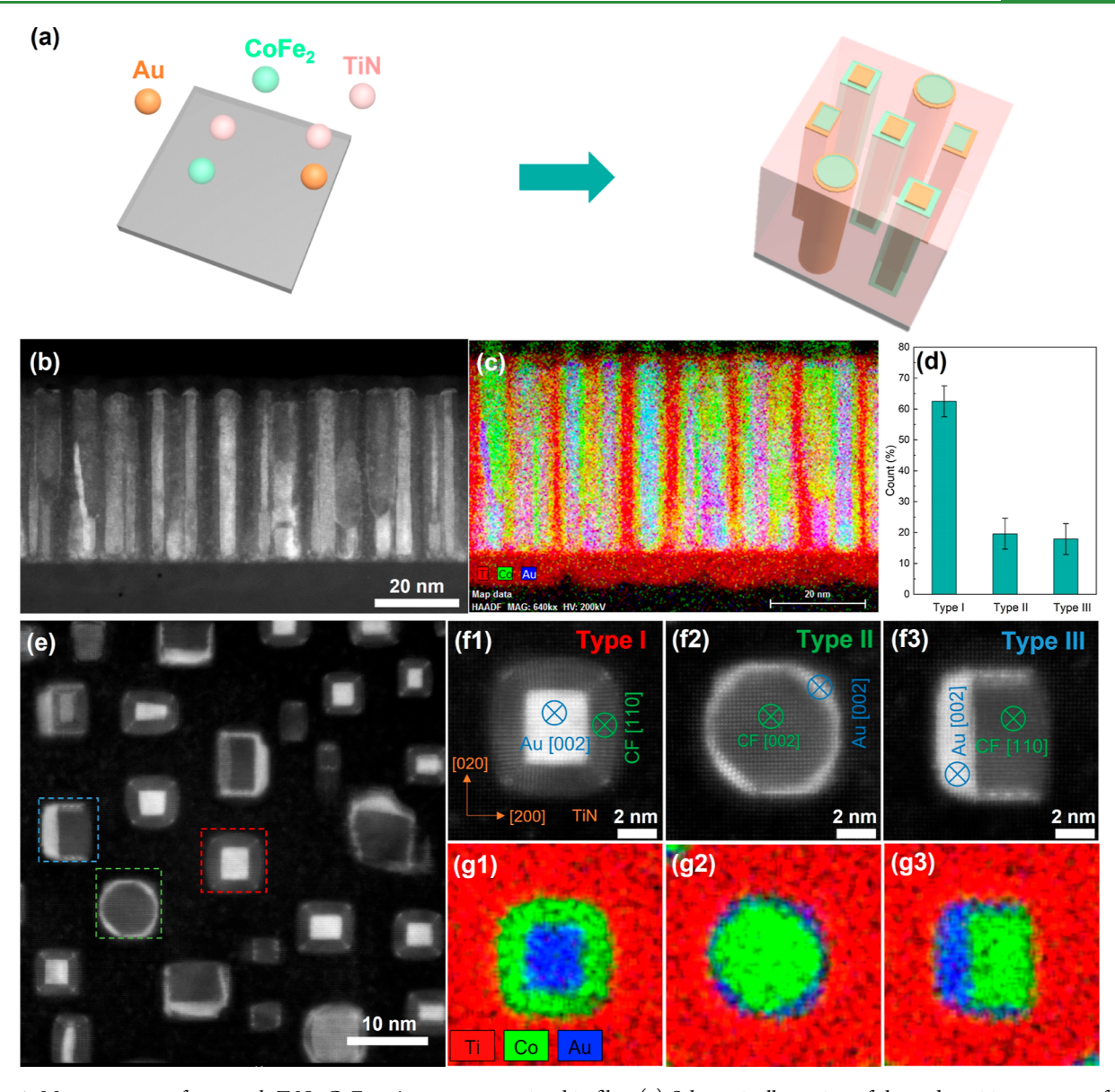


Figure 1. Microstructure of cogrowth  $TiN-CoFe_2$ —Au nanocomposite thin film. (a) Schematic illustration of the codeposition process of  $TiN-CoFe_2$ —Au nanocomposites; (b) cross-sectional STEM images of  $TiN-CoFe_2$ —Au nanocomposites; (c) cross-sectional EDS images of  $TiN-CoFe_2$ —Au nanocomposites; (d) distribution analysis of three types of nanopillar configurations; (e) low-magnification plan-view STEM images of  $TiN-CoFe_2$ —Au nanocomposites; (f) high-magnification plan-view STEM images of one representative nanopillar for type I (f1), type II (f2), and type III (f3); and (g) corresponding EDS images of one representative nanopillar for type I (g1), type II (g2), and type III (g3).

rials in a thin-film form. By using a one-step PLD deposition technique, two different phases can self-assemble into a hybrid structure (e.g., pillar-in-matrix and nanocheckerboard). VANs have been demonstrated in various materials systems, such as oxide-oxide systems, <sup>25,26</sup> oxide-metal systems, <sup>27</sup> and nitridemetal systems.<sup>28</sup> Considering the plasmonic properties of nitrides, incorporating ferromagnetic components into the nitride matrix is a promising platform for forming magnetooptic metamaterials.<sup>29-31</sup> Besides the two-phase VAN structure, some three-phase nanocomposite thin films (TiN-Au-NiO, 30 BaTiO<sub>3</sub>-Au-Co, 32 and La<sub>0.5</sub>Sr<sub>0.5</sub>FeO<sub>3</sub>-Au-Fe<sup>33</sup>) have also been successfully deposited into the VAN form. Detailed microstructure analysis of those three-phase nanocomposites reveals a VAN structure with two-phase core-shell nanopillars, which naturally generate magnetic-plasmonic coupled interfaces, thus enhancing MO coupling effects.

In this work, we report a novel complex three-phase nitridebased hybrid material. Here, TiN is chosen as the matrix due to its plasmonic properties, good lattice matching and wettability on the MgO substrate, and high durability. Au and CoFe<sub>2</sub> phases are metallic phases selected as the coreshell structure considering their plasmonic and ferromagnetic properties. Due to the high surface energy of metals, as well as their immiscibility of Au and Co/Fe, Au-CoFe<sub>2</sub> is expected to form a core-shell structure in the TiN matrix. In this way, a MO coupling effect can be generated at CoFe<sub>2</sub> phases as well as their interfaces with TiN and Au. Owing to the unique VAN morphology, TiN-CoFe<sub>2</sub>-Au nanocomposites could also exhibit strong anisotropic optical and magnetic responses. We adopted two different approaches in processing this complex three-phase system, a codeposition method and a templated growth method. Specifically, the codeposition method deposits all three phases simultaneously as illustrated

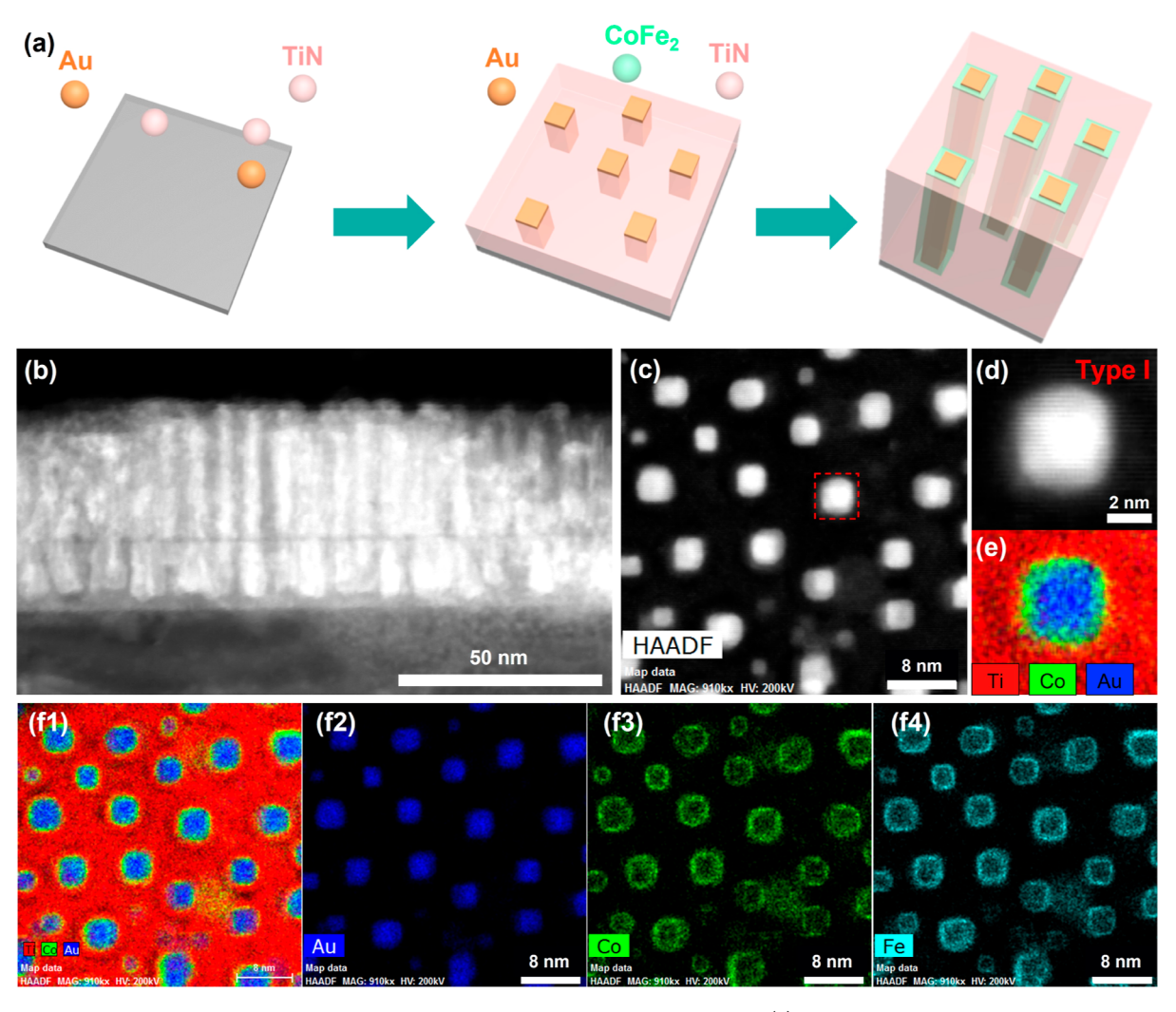


Figure 2. Microstructure of templated growth TiN-CoFe<sub>2</sub>-Au nanocomposite thin film. (a) Schematic illustration of the templated growth process of TiN-CoFe<sub>2</sub>-Au nanocomposites; (b) cross-sectional STEM images of TiN-CoFe<sub>2</sub>-Au nanocomposites; (c) plan-view images of TiN-CoFe<sub>2</sub>-Au nanocomposites; (d) high-magnification plan-view STEM images of one representative nanopillar; (e) corresponding EDS images of one representative nanopillar; and (f) low-magnification plan-view EDS images of TiN-CoFe<sub>2</sub>-Au nanocomposites.

in Figure 1a, while the templating method uses a TiN-Au seed layer to grow TiN-CoFe<sub>2</sub> to enhance the uniformity of the core—shell nanopillars as illustrated in Figure 2. Self-assembly and growth mechanisms for both cases are proposed based on the observed microstructures. The optical, magnetic, and MO coupling properties of these two structures were measured and compared. These self-assembled methods could be applied to ease the complex fabrication of multiphase metamaterials with better controlled morphologies, anisotropic physical properties, and unique functionality coupling effects that could not be easily achieved otherwise.

#### RESULTS AND DISCUSSION

The three-phase TiN–CoFe<sub>2</sub>–Au nanocomposite films were first characterized by X-ray diffraction (XRD). As shown in Figure S1 (Supporting Information), the TiN phase in both cogrowth sample and templated sample is textured along (002). The CoFe<sub>2</sub> phase shows two growth orientations, i.e., (011) and (002) in the cogrowth sample, while only the (002) peak can be observed in the templated sample. Since Au(002) and CoFe<sub>2</sub>(011) have similar d-spacings ( $d_{\rm Au(002)} = 2.036$  Å,  $d_{\rm CoFe,(011)} = 2.025$  Å), Au(002) peak is

overlapped with  $CoFe_2(011)$  on the right side of the MgO substrate peak. The peak splitting in  $CoFe_2(011)$  can be attributed to different strain states of the  $CoFe_2$  phase, which will be discussed along with the following microstructure characterization results. Compared to the cogrowth sample, the templated sample shows fewer  $CoFe_2$  peaks and less peak splitting which suggests a higher uniformity of the  $CoFe_2$  phase.

To further investigate the detailed microstructure of the  $TiN-CoFe_2$ —Au three-phase nanocomposite thin film, we use scanning transmission electron microscopy (STEM) and energy-dispersive X-ray spectroscopy (EDS). Figure 1a presents a schematic illustration of the codeposition growth process. The cross-sectional STEM image (Figure 1b) and corresponding EDS images (Figure 1c) reveal a clear pillar-inmatrix morphology in the codeposited  $TiN-CoFe_2$ —Au nanocomposite film. The clear and sharp interfaces suggest a high crystallinity in the three-phase nanocomposite thin film. Since the contrast is proportional to the atomic number (i.e.,  $\sim Z^{1.7}$ ),  $^{34-36}$  the Au phase ( $Z_{Au}=79$ ) is brighter than the  $CoFe_2$  phase ( $Z_{Co}=27$ ,  $Z_{Fe}=26$ ). The contrast difference in the pillar region suggests that  $CoFe_2$  and Au phases grow separately and form a core–shell nanopillar. The plan-view

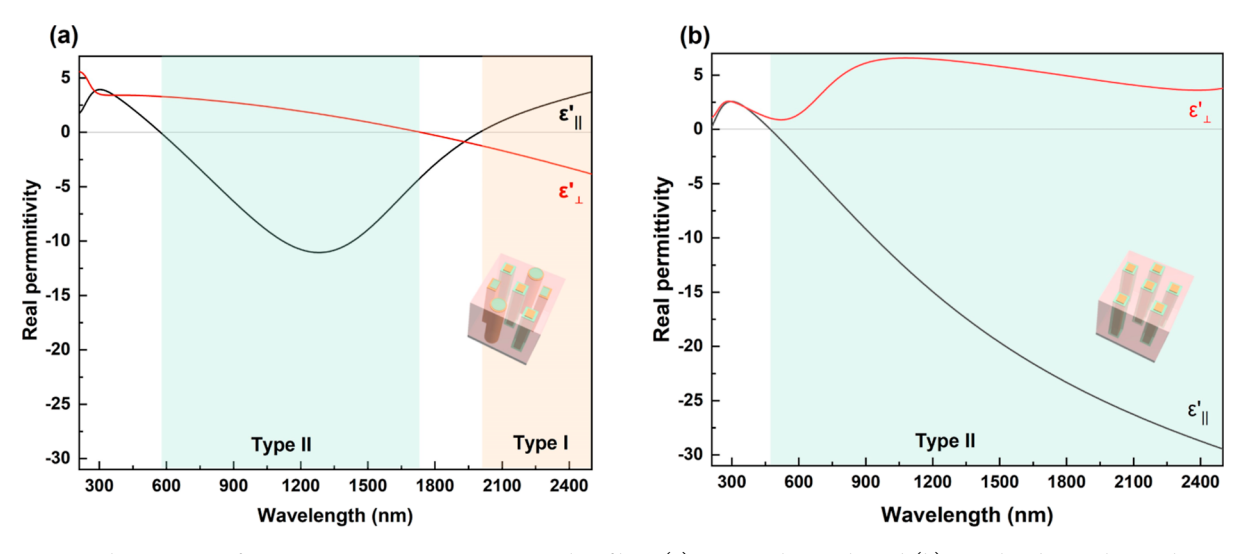


Figure 3. Optical properties of TiN-CoFe<sub>2</sub>-Au nanocomposite thin films. (a) Cogrowth sample and (b) templated growth sample.

image of the cogrowth sample in Figure 2e can further confirm that each pillar has a core-shell structure. Interestingly, these core-shell nanopillars are randomly distributed in the TiN matrix and display different configurations. Here, we analyzed the configurations of all of the nanopillars in a lowmagnification plan-view STEM image (Figure S2) and categorized them into three types (i.e., type I, type II, and type III). As shown in the plan-view EDS mapping of three representative nanopillars (Figure 1g1-3), type I pillars (boxed with red-dashed lines in Figure 1e) have inner Au cores and outer CoFe<sub>2</sub> shells, type II pillars (boxed with greendashed lines in Figure 1e) have inner CoFe<sub>2</sub> cores with Au shells, and type III pillars (boxed with blue-dashed lines in Figure 1e) have half-shaped Au shells circled with CoFe<sub>2</sub> cores. As these nanostructures resemble some of the gemstone cuts or special shapes, we named them nanoasshers, nanorounds, and nanocombs for type I, II, and III, respectively. The distribution of these three types of pillars is plotted in Figure 1d, suggesting that type I configuration is more dominant (62.5%) compared to type II (19.6%) and type III (17.9%).

The complex three-phase core-shell VAN structure is believed to result from the interplay of surface energy, interface energy, and lattice mismatch. First, the nucleation and growth mode of each phase largely depend on surface energy. To aid the discussion, Table S1 summarizes the lattice parameters and surface energy of Au, CoFe2, TiN, and MgO in different orientations. Both metallic Au and CoFe<sub>2</sub> have a larger surface energy compared to MgO and thus prefer a Volmer-Weber 3D island growth mode and finally grow into nanopillars. TiN has a surface energy comparable to that of MgO, which follows the layer-by-layer (2D Frank-van der Merve) growth mode and thus forms the matrix. The strain energy induced by the lattice mismatch can also contribute to the nucleation and growth modes observed. Since the difference in surface energy is relatively large, the strain energy effect could be neglected in determining the growth model in this case. Second, since the interfacial energy of metal-metal interface is lower than metal-ceramic interface, Au and CoFe<sub>2</sub> phase favors a coreshell structure instead of separate nanopillars to minimize interface energy. It is also interesting to study the origin of three types of configurations (i.e., type I, type II, and type III) for Au-CoFe<sub>2</sub> nanopillars. Figure 2f1-3 presents atomic-scale plan-view STEM images of one representative nanopillar for

each type. It is found that the CoFe<sub>2</sub> phase exposes both (110) and (002) facets, while the other two phases (Au and TiN) only expose (002) facets. During the initial nucleation stage, CoFe<sub>2</sub> nucleates both (110) and (002) simultaneously. Notice that  $CoFe_2(002)$  has a large lattice mismatch with Au(002)and matrix TiN(002), while CoFe<sub>2</sub>(011) can match well with Au(002) and TiN(002) well. For mismatched CoFe<sub>2</sub>(002) orientation, Au prefers to grow encircling around CoFe2 and form an outer shell to minimize highly strained interfaces and reduce the strain energy (type II). If CoFe<sub>2</sub> nucleates as matched (011) orientation, Au grows as either the inner (type I) core or the outer half shell (type III). Furthermore, it is worth noting that both type I and type II are centrosymmetric while type III is noncentrosymmetric. These structural differences between centrosymmetric and noncentrosymmetric structures are primarily attributed to the growth orientation. In the case of type I and II core-shell structures, both the Au(002) core and the  $CoFe_2(002)$  core are centrosymmetric, as illustrated in Figure S4c,d. Consequently, their growth orientation results in a symmetric configuration. Conversely, for the type III core-shell structure, the core is CoFe<sub>2</sub>(110), which is not symmetric as shown in Figure S4f. That naturally causes the CoFe<sub>2</sub>(110) core to grow asymmetrically and to have a rectangular in-plane shape. A similar phenomenon has been observed in previously reported TiN-CoFe<sub>2</sub> nanocomposites. Moreover, due to the relatively smaller lattice mismatch between CoFe<sub>2</sub>[110]//Au[200] and CoFe<sub>2</sub>[200]// Au[200], the Au phase tends to attach preferentially to the long edge of the CoFe2 core rather than the short edge. Consequently, this preference ultimately gives rise to the formation of the nonsymmetric type III core—shell structure.

To precisely control the microstructure of TiN-CoFe<sub>2</sub>-Au nanocomposite film with more uniform core-shell nanopillars, we adopted a template growth method to enhance the ordering and uniformity of the pillar configuration. As shown in Figure 2a, a TiN-Au seed layer was first deposited on the MgO substrate and then the coming Au adatoms prefer to directly nucleate on top of Au seeds and finally form the Au core. In this way, the large mismatched CoFe<sub>2</sub>(002) can be avoided and therefore all nanopillars have type I configuration. The cross-section and plan-view STEM images of the templated sample in Figure 2b,c show expected core-shell nanopillars vertically aligned in the TiN matrix. Plan-view EDS images

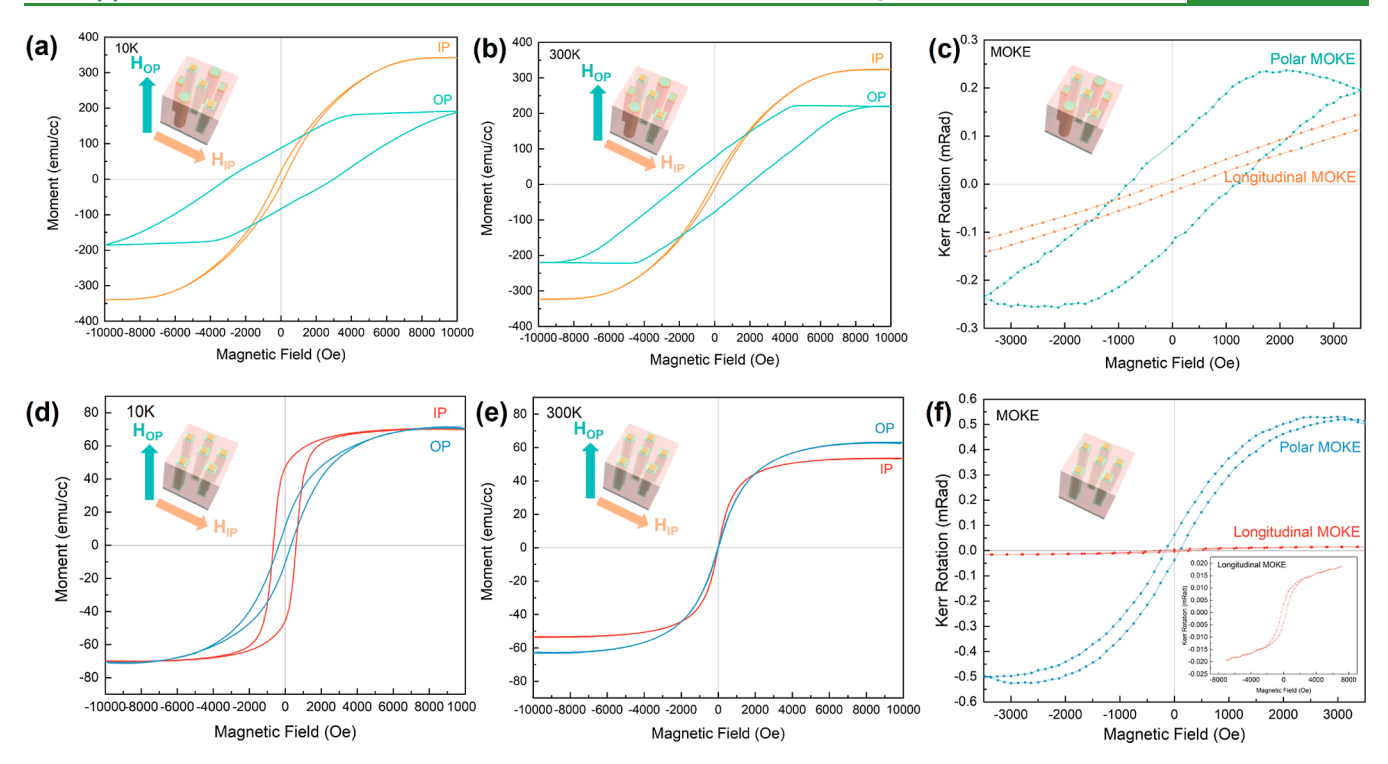


Figure 4. Magnetic properties and MO coupling effect in TiN-CoFe<sub>2</sub>-Au nanocomposite thin films. (a) Comparison of in-plane and out-of-plane M-H hysteresis loops of cogrowth TiN-CoFe<sub>2</sub>-Au nanocomposites at 10 K; (b) comparison of in-plane and out-of-plane M-H hysteresis loops of cogrowth TiN-CoFe<sub>2</sub>-Au nanocomposites at 300 K; (c) polar and longitudinal Kerr rotation of cogrowth TiN-CoFe<sub>2</sub>-Au nanocomposites; (d) comparison of in-plane and out-of-plane M-H hysteresis loops of templated growth TiN-CoFe<sub>2</sub>-Au nanocomposites at 10 K; (e) comparison of in-plane and out-of-plane M-H hysteresis loops of templated TiN-CoFe<sub>2</sub>-Au nanocomposites at 300 K; and (f) polar and longitudinal Kerr rotation of templated growth TiN-CoFe<sub>2</sub>-Au nanocomposites.

(Figure 2f1–4) confirm all nanopillars display a type-I (Au core in  $CoFe_2$  shell) core—shell structure. The Co and Fe elements detected in the bottom seed layers (Figure S3) suggest that the type-I core—shell structure is maintained throughout the film, which is attributed to the interdiffusion during the high-temperature deposition process. It is also worth mentioning that the thickness of  $CoFe_2$  shell in the templated growth sample ( $\sim$ 0.675 nm) is thinner than that in the cogrowth sample ( $\sim$ 1.575 nm). This can be explained by the presence of  $CoFe_2$  in the buffer layer.

The change in microstructures could have a remarkable effect on the light-matter interaction and thus the overall optical response of metamaterial thin films. Therefore, we conducted ellipsometry measurements on both cogrowth and templated growth samples. The real permittivity was retrieved from fitted ellipsometric parameters and plotted in Figure 3a,b for the cogrowth and the templated growth samples, respectively. The in-plane and out-of-plane permittivities were plotted separately considering the anisotropic nature of the films. It can be seen that both the cogrowth sample and the templated growth sample display highly anisotropic optical responses and exhibit hyperbolic dispersion due to their anisotropic microstructure. The green-shaded area represents the type II hyperbolic region, and the orange-shaded area represents the type I hyperbolic region. The real permittivity of the cogrowth sample displays two hyperbolic dispersion regions, i.e., type II hyperbolic dispersion from 600 to 1700 nm and type I hyperbolic dispersion over 2000 nm. In the templated sample, the out-of-plane permittivity is positive in the entire wavelength ranging from 210 to 2500 nm, while the in-plane permittivity decreases from a positive to negative

region with the epsilon-near-zero point in the visible regime at 470 nm. This results in type II hyperbolic behavior in most visible and NIR regions.

Since the CoFe<sub>2</sub> alloy is a well-known ferromagnetic material, it is worth investigating the magnetic properties of the three-phase TiN-CoFe<sub>2</sub>-Au thin films. To study the anisotropy of the films, the magnetic measurement was conducted with the field applied perpendicular (out-of-plane, OP) and parallel (in-plane, IP) to the film surface separately. The M-H hysteresis loops of the cogrowth sample at 10 K in Figure 4a show a strong ferromagnetic response and OP magnetic anisotropy. More specifically, the coercive field is 2851 Oe for OP and 74 Oe for IP, respectively. This magnetic anisotropy is mainly from the anisotropic shape of CoFe<sub>2</sub>-Au nanopillars, which is commonly seen in magnetic VAN films.<sup>37</sup> The M-H loops measured at room temperature (Figure 4b) display characteristics similar to those of 10 K (i.e., ferromagnetic response and OP magnetic anisotropy), with a lower coercive field due to higher thermal energy. The magnetic property measurement was also conducted on the templated growth sample at 10 K and room temperature (Figure 4d,e). Compared to the cogrowth sample, the templated growth sample shows a weaker ferromagnetic response as well as magnetic anisotropy. This is mainly because the magnetic CoFe2 shells are thinner than that in the cogrowth sample. Interestingly, it was observed that the IP coercive field is larger than the OP coercive field in the templated growth sample. This suggests that the magnetic easy axis was changed from OP direction in the cogrowth sample to IP direction in the templated growth sample. Magnetic anisotropy usually depends on magnetocrystalline anisotropy,

shape anisotropy, and stress anisotropy. To a single-crystal  $CoFe_2$  with a cubic structure, the easy axis is  $\langle 001 \rangle$ , which is the IP orientation in the templated sample. This indicates that the magnetocrystalline anisotropy overcomes shape and stress anisotropy by uniforming all nanopillars into the type I configuration. This method is of great interest to precisely control the magnetic easy axis in magnetic nanocomposite thin films, which helps in future magnetic recording devices or other applications.

In order to investigate the potential coupling effect between the magnetic CoFe2 and the plasmonic TiN and Au, MO Kerr effect (MOKE) measurements were performed on both the cogrowth and templated growth samples using two configurations: polar MOKE and longitudinal MOKE. Polar MOKE (P-MOKE) employed a perpendicular magnetic field with a normal incident laser, while longitudinal MOKE (L-MOKE) utilized a parallel magnetic field and a 60° laser. Both samples present MOKE responses, as shown in Figure 4c,f. The cogrowth sample also exhibits wider Kerr rotation hysteresis loops in both polar and longitudinal configurations compared to the templated sample, which consists of the result in magnetic property measurements. It should be noted that due to the limitations of the equipment setup, the applied field range in the polar MOKE configuration was limited to -3500to 3500 Oe, which resulted in a weaker P-MOKE signal than expected. With this limitation, the MOKE signal is still significantly more pronounced along OP direction (polar MOKE) than the IP direction (longitudinal MOKE) for both samples. This difference can be attributed to the MO coupling effect arising from the vertical CoFe<sub>2</sub> phase and the vertical CoFe<sub>2</sub>-TiN and CoFe<sub>2</sub>-Au interfaces. Furthermore, the difference between the P-MOKE and L-MOKE signals in the templated sample (Figure 4f) is significantly greater than that in the cogrowth sample (Figure 4c), which suggests that the CoFe<sub>2</sub>-TiN interfaces and CoFe<sub>2</sub>-Au interfaces also contribute to the MOKE response since the templated sample has a much higher density of those vertical interfaces.

Overall, these three-phase nanocomposites present a complex microstructure with vertically aligned CoFe<sub>2</sub>-Au core-shell nanopillars embedded in the TiN matrix. Enhanced uniformity of the core-shell pillars was achieved by applying a template layer. This finding is fundamentally important for studying the growth mechanism of the self-assembling process, as well as the effects of surface energy and strain energy in multiphase thin-film growth, which opens up possibilities in precisely controlling the morphology and achieving highly ordered nanopillars by such a self-assembled growth method. In addition to template layers, the microstructure of the multiphase thin film can be further tailored by the substrate selection and varying deposition parameters (i.e., growth temperature, laser frequency, etc.). This versatility allows for systematic manipulation of the microstructural characteristics, thereby enabling the tuning of optical and magnetic properties in a highly controllable manner. Furthermore, compared with a previous study of the two-phase TiN-CoFe2 nanocomposites,<sup>39</sup> this three-phase design offers more flexibility in microstructure and therefore results in more tunable optical and magnetic properties, such as realizing diverse hyperbolic dispersion and manipulating the switching magnetic easy axis.

#### CONCLUSIONS

In summary, we have demonstrated a self-assembled nanostructured three-phase TiN-CoFe<sub>2</sub>-Au nanocomposite design

by using two methods, i.e., the codeposition and the templated growth. Microstructure characterizations reveal three different types of core-shell CoFe<sub>2</sub>-Au nanopillars that are vertically aligned in the TiN matrix for the codeposition sample. Significant enhancement in the uniformity of the CoFe<sub>2</sub>-Au nanopillar configuration has been achieved by applying the TiN-Au seed layer in the templated growth sample. The three-phase nanocomposites exhibit highly anisotropic optical and magnetic responses which can be further tuned by precisely controlling the microstructure. This nanocomposite design enables an effective combination of ferromagnetic CoFe<sub>2</sub> with plasmonic TiN and Au, which produce pronounced OP MO coupling effects. This work provides a better understanding of the combined effects between surface energy and strain energy during the self-assembly process of the multiphase thin films which leads to uniform metamaterial designs. The work also presents a promising platform for designing complex multiphase magneto-optic hybrid materials toward future MO memories, optical isolators, and light modulators.

#### EXPERIMENTAL SECTION

**Thin-Film Growth.** The TiN–CoFe<sub>2</sub>O<sub>4</sub>–Au target consists of pie-shaped CoFe<sub>2</sub>O<sub>4</sub>, short Au strip, and TiN targets. The nanocomposite films were grown on MgO (001) substrates by pulsed laser deposition with a KrF excimer laser (Lambda Physik Compex Pro 205,  $\lambda$  = 248 nm). Deposition temperature was 700 °C and the chamber was kept at a high vacuum condition (1.0 × 10<sup>-6</sup> mbar) during the deposition and cooling processes.

**Structural Characterizations.** The crystallinity was characterized by XRD (Panalytical X'Pert X-ray diffractometer) with a Cu K $\alpha$ 1 radiation source ( $\lambda$  = 0.15406 nm). Transmission electron microscopy (TEM) and STEM [under a high-angle annular dark field (HAADF) mode] were taken on a Thermo Fisher Scientific (FEI) Talos F200X system with a point-to-point resolution of 1.6 Å. A FEI TitanTM G2 80–200 scanning transmission electron microscope with a Cs probe corrector and ChemiSTEM technology (X-FEGTM and SuperXTM EDS with four windowless silicon drift detectors) operated at 200 kV was used for high-resolution HAADF—STEM imaging and EDS analysis. The TEM samples were prepared by a standard procedure, including manual grinding, polishing, dimpling, and a final ion milling step (PIPS 695 precision ion polishing system, Gatan Inc.).

**Optical Characterizations.** Spectroscopic ellipsometry measurements were carried out with a Woollam RC2 ellipsometer. The ellipsometry parameters psi  $(\Psi)$  and delta  $(\Delta)$  were collected at variable angles (55, 65, and  $75^{\circ})$  and a spectrum range from 210 to 2500 nm. An AEp uniaxial model was built with Gen-Osc oscillators to fit ellipsometer parameters in CompleteEASE software. Transmittance spectra were measured on a UV–vis–NIR absorption spectrophotometer (PerkinElmer Lambda 1050).

Magnetic Characterization. The magnetic hysteresis loops were measured by a Quantum Design MPMS-3 SQUID magnetometer with the vibrating sample magnetometer mode. The magneto-optic (MOKE) measurements were carried out by a home-built MOKE system with two configurations (polar and longitudinal). A laser with a wavelength of 632 nm was applied as a source light, and the magnetic field was in the range of -3500 to 3500 Oe for P-MOKE and -7000 to 7000 Oe for L-MOKE.

#### ASSOCIATED CONTENT

#### Supporting Information

The Supporting Information is available free of charge at https://pubs.acs.org/doi/10.1021/acsami.3c06777.

Lattice parameter and surface energy of Au, CoFe<sub>2</sub>, TiN, MgO; XRD  $\theta$ –2 $\theta$  scans; low-magnification STEM images of cogrowth TiN–CoFe<sub>2</sub>–Au nanocomposites;

cross-sectional EDS images of templated growth TiN-CoFe<sub>2</sub>-Au nanocomposites; and crystal structures of Au and CoFe<sub>2</sub> (PDF)

#### AUTHOR INFORMATION

#### **Corresponding Author**

Haiyan Wang — School of Materials Engineering, Purdue University, West Lafayette, Indiana 47907, United States; School of Electrical and Computer Engineering, Purdue University, West Lafayette, Indiana 47907, United States; orcid.org/0000-0002-7397-1209; Email: hwang00@purdue.edu

#### **Authors**

Jiawei Song — School of Materials Engineering, Purdue University, West Lafayette, Indiana 47907, United States Di Zhang — School of Materials Engineering, Purdue University, West Lafayette, Indiana 47907, United States; Center for Integrated Nanotechnologies (CINT), Los Alamos National Laboratory, Los Alamos, New Mexico 87545, United States; orcid.org/0000-0002-9199-5634

Ping Lu — Sandia National Laboratories, Albuquerque, New Mexico 87185, United States

Yizhi Zhang – School of Materials Engineering, Purdue University, West Lafayette, Indiana 47907, United States

Haohan Wang — Department of Physics and Astronomy, University of Nebraska—Lincoln, Lincoln, Nebraska 68588, United States

Hongyi Dou – School of Materials Engineering, Purdue University, West Lafayette, Indiana 47907, United States

Xiaoshan Xu — Department of Physics and Astronomy, University of Nebraska—Lincoln, Lincoln, Nebraska 68588, United States; oorcid.org/0000-0002-4363-392X

Julia Deitz – Sandia National Laboratories, Albuquerque, New Mexico 87185, United States

Xinghang Zhang — School of Materials Engineering, Purdue University, West Lafayette, Indiana 47907, United States; orcid.org/0000-0002-8380-8667

Complete contact information is available at: https://pubs.acs.org/10.1021/acsami.3c06777

#### Notes

The authors declare no competing financial interest.

#### ACKNOWLEDGMENTS

This work was supported by the U.S. National Science Foundation DMR-2016453. The microscopy work was partially supported by the Laboratory Directed Research and Development program at Sandia National Laboratories. Sandia National Laboratories is a multimission laboratory managed and operated by National Technology and Engineering Solutions of Sandia, LLC., a wholly owned subsidiary of Honeywell International, Inc., for the U.S. Department of Energy's National Nuclear Security Administration under contract no. DE-NA0003525. The MOKE studies were supported by NSF EPSCoR RII Track-1: Emergent Quantum Materials and Technologies (EQUATE), award no. OIA-2044049. This paper describes objective technical results and analysis. The work at Los Alamos National Laboratory was supported by the NNSA's Laboratory Directed Research and Development Program and was performed, in part, at the Center for Integrated Nanotechnologies, an Office of Science

User Facility operated for the U.S. Department of Energy Office of Science. Los Alamos National Laboratory, an affirmative action equal opportunity employer, is managed by Triad National Security, LLC for the U.S. Department of Energy's NNSA, under contract 89233218CNA000001. Any subjective views or opinions that might be expressed in the paper do not necessarily represent the views of the U.S. Department of Energy or the United States Government.

#### REFERENCES

- (1) el Hadri, M. S.; Pirro, P.; Lambert, C. H.; Petit-Watelot, S.; Quessab, Y.; Hehn, M.; Montaigne, F.; Malinowski, G.; Mangin, S. Two Types of All-Optical Magnetization Switching Mechanisms Using Femtosecond Laser Pulses. *Phys. Rev. B* **2016**, *94* (6), 064412–064418.
- (2) Zhang, P.; Chung, T. F.; Li, Q.; Wang, S.; Wang, Q.; Huey, W. L. B.; Yang, S.; Goldberger, J. E.; Yao, J.; Zhang, X. All-Optical Switching of Magnetization in Atomically Thin CrI3. *Nat. Mater.* **2022**, *21*, 1373–1378.
- (3) Tudu, B.; Tiwari, A. Recent Developments in Perpendicular Magnetic Anisotropy Thin Films for Data Storage Applications. *Vacuum* **2017**, *146*, 329–341.
- (4) Tudosa, I.; Stamm, C.; Kashuba, A. B.; King, F.; Siegmann, H. C.; Stöhr, J.; Ju, G.; Lu, B.; Weller, D. The Ultimate Speed of Magnetic Switching in Granular Recording Media. *Nature* **2004**, 428 (6985), 831–833.
- (5) Hu, S.; Shao, D. F.; Yang, H.; Pan, C.; Fu, Z.; Tang, M.; Yang, Y.; Fan, W.; Zhou, S.; Tsymbal, E. Y.; Qiu, X. Efficient Perpendicular Magnetization Switching by a Magnetic Spin Hall Effect in a Noncollinear Antiferromagnet. *Nat. Commun.* 2022, 13 (1), 4447.
- (6) Maccaferri, N.; Zubritskaya, I.; Razdolski, I.; Chioar, I. A.; Belotelov, V.; Kapaklis, V.; Oppeneer, P. M.; Dmitriev, A. Nanoscale magnetophotonics. *J. Appl. Phys.* **2020**, *127* (8), 080903.
- (7) Haider, T. A Review of Magneto-Optic Effects and Its Application. *Int. J. Electromagn. Appl.* **2017**, 7 (1), 17–24.
- (8) Rizal, C.; Manera, M. G.; Ignatyeva, D. O.; Mejía-Salazar, J. R.; Rella, R.; Belotelov, V. I.; Pineider, F.; MacCaferri, N. Magnetophotonics for Sensing and Magnetometry toward Industrial Applications. *J. Appl. Phys.* **2021**, *130* (23), 230901 DOI: 10.1063/5.0072884.
- (9) Krusin-Elbaum, L.; Shibauchi, T.; Argyle, B.; Gignac, L.; Weller, D. Stable Ultrahigh-Density Magneto-Optical Recordings Using Introduced Linear Defects The Stability of Data Bits in Magnetic Recording Media. *Nature* **2001**, *410*, 444.
- (10) Pourjamal, S.; Kataja, M.; Maccaferri, N.; Vavassori, P.; van Dijken, S. Tunable Magnetoplasmonics in Lattices of Ni/SiO2/Au Dimers. *Sci. Rep.* **2019**, 9 (1), 9907 DOI: 10.1038/s41598-019-46058-2
- (11) Sepúlveda, B.; Calle, A.; Lechuga, L. M.; Armelles, G. Highly Sensitive Detection of Biomolecules with the Magneto-Optic Surface-Plasmon-Resonance Sensor. *Opt. Lett.* **2006**, *31*, 1085.
- (12) González-Díaz, J. B.; García-Martín, A.; García-Martín, J. M.; Cebollada, A.; Armelles, G.; Sepúlveda, B.; Alaverdyan, Y.; Käll, M. Plasmonic Au/Co/Au Nanosandwiches with Enhanced Magneto-Optical Activity. *Small* **2008**, *4* (2), 202–205.
- (13) Newman, D. M.; Wears, M. L.; Matelon, R. J.; Hooper, I. R. Magneto-Optic Behaviour in the Presence of Surface Plasmons. *J. Phys.: Condens. Matter* **2008**, *20* (34), 345230.
- (14) Grunin, A. A.; Zhdanov, A. G.; Ezhov, A. A.; Ganshina, E. A.; Fedyanin, A. A. Surface-Plasmon-Induced Enhancement of Magneto-Optical Kerr Effect in All-Nickel Subwavelength Nanogratings. *Appl. Phys. Lett.* **2010**, *97* (26), 261908 DOI: 10.1063/1.3533260.
- (15) Hermann, C.; Kosobukin, V. A.; Lampel, G.; Peretti, J.; Safarov, V. I.; Bertrand, P. Surface-Enhanced Magneto-Optics in Metallic Multilayer Films. *Phys. Rev. B: Condens. Matter Mater. Phys.* **2001**, 64 (23), 235422–235511.
- (16) López-Ortega, A.; Zapata-Herrera, M.; Maccaferri, N.; Pancaldi, M.; Garcia, M.; Chuvilin, A.; Vavassori, P. Enhanced Magnetic

- Modulation of Light Polarization Exploiting Hybridization with Multipolar Dark Plasmons in Magnetoplasmonic Nanocavities. *Light: Sci. Appl.* **2020**, *9* (1), 49.
- (17) Wang, L.; Clavero, C.; Huba, Z.; Carroll, K. J.; Carpenter, E. E.; Gu, D.; Lukaszew, R. A. Plasmonics and Enhanced Magneto-Optics in Core-Shell Co-Ag Nanoparticles. *Nano Lett.* **2011**, *11* (3), 1237–1240
- (18) Naik, G.; Kim, J.; Kinsey, N.; Boltasseva, A. Alternative Plasmonic Materials. *Handb. Surf. Sci.* **2014**, *4*, 189–221, DOI: 10.1016/B978-0-444-59526-3.00006-9.
- (19) Guler, U.; Shalaev, V. M.; Boltasseva, A. Nanoparticle Plasmonics: Going Practical with Transition Metal Nitrides. *Mater. Today* **2015**, *18* (4), 227–237.
- (20) Li, W.; Guler, U.; Kinsey, N.; Naik, G. V.; Boltasseva, A.; Guan, J.; Shalaev, V. M.; Kildishev, A. V. Refractory Plasmonics with Titanium Nitride: Broadband Metamaterial Absorber. *Adv. Mater.* **2014**, *26* (47), 7959–7965.
- (21) Guo, W. P.; Mishra, R.; Cheng, C. W.; Wu, B. H.; Chen, L. J.; Lin, M. T.; Gwo, S. Titanium Nitride Epitaxial Films as a Plasmonic Material Platform: Alternative to Gold. ACS Photonics 2019, 6 (8), 1848–1854.
- (22) Kuttruff, J.; Gabbani, A.; Petrucci, G.; Zhao, Y.; Iarossi, M.; Pedrueza-Villalmanzo, E.; Dmitriev, A.; Parracino, A.; Strangi, G.; de Angelis, F.; Brida, D.; Pineider, F.; Maccaferri, N. Magneto-Optical Activity in Nonmagnetic Hyperbolic Nanoparticles. *Phys. Rev. Lett.* **2021**, *127* (21), 217402.
- (23) Rowan-Robinson, R. M.; Hurst, J.; Ciuciulkaite, A.; Chioar, I.-A.; Pohlit, M.; Zapata-Herrera, M.; Vavassori, P.; Dmitriev, A.; Oppeneer, P. M.; Kapaklis, V. Direction-Sensitive Magnetophotonic Surface Crystals. *Adv. Photonics Res.* **2021**, *2* (10), 2100119.
- (24) Petrucci, G.; Gabbani, A.; Faniayeu, I.; Pedrueza-Villalmanzo, E.; Cucinotta, G.; Atzori, M.; Dmitriev, A.; Pineider, F. Macroscopic Magneto-Chiroptical Metasurfaces. *Appl. Phys. Lett.* **2021**, *118* (25), 251108.
- (25) Sun, X.; MacManus-Driscoll, J. L.; Wang, H. Spontaneous Ordering of Oxide-Oxide Epitaxial Vertically Aligned Nanocomposite Thin Films. *Annu. Rev. Mater. Res.* **2020**, *50*, 229–253.
- (26) Chen, A.; Jia, Q. A Pathway to Desired Functionalities in Vertically Aligned Nanocomposites and Related Architectures. *MRS Bull.* **2021**, 46 (2), 115–122.
- (27) Zhang, D.; Wang, H. Self-Assembled Metal–Dielectric Hybrid Metamaterials in Vertically Aligned Nanocomposite Form with Tailorable Optical Properties and Coupled Multifunctionalities. *Adv. Photonics Res.* **2021**, 2 (5), 2000174.
- (28) Wang, X.; Wang, H. Self-Assembled Nitride-Metal Nanocomposites: Recent Progress and Future Prospects. *Nanoscale* **2020**, 12 (40), 20564–20579.
- (29) Kalaswad, M.; Zhang, D.; Rutherford, B. X.; Lu, J.; Barnard, J. P.; He, Z.; Liu, J.; Wang, H.; Xu, X.; Wang, H. TiN—Fe Vertically Aligned Nanocomposites Integrated on Silicon as a Multifunctional Platform toward Device Applications. *Crystals* **2022**, *12* (6), 849 DOI: 10.3390/cryst12060849.
- (30) Wang, X.; Jian, J.; Wang, H.; Liu, J.; Pachaury, Y.; Lu, P.; Rutherford, B. X.; Gao, X.; Xu, X.; El-Azab, A.; Zhang, X.; Wang, H. Nitride-Oxide-Metal Heterostructure with Self-Assembled Core—Shell Nanopillar Arrays: Effect of Ordering on Magneto-Optical Properties. *Small* **2021**, *17* (5), 2007222–2007229.
- (31) Wang, X.; Wang, H.; Jian, J.; Rutherford, B. X.; Gao, X.; Xu, X.; Zhang, X.; Wang, H. Metal-Free Oxide-Nitride Heterostructure as a Tunable Hyperbolic Metamaterial Platform. *Nano Lett.* **2020**, *20* (9), 6614–6622.
- (32) Huang, J.; Phuah, X. L.; McClintock, L. M.; Padmanabhan, P.; Vikrant, K. S. N.; Wang, H.; Zhang, D.; Wang, H.; Lu, P.; Gao, X.; Sun, X.; Xu, X.; Edwin García, R.; Chen, H. T.; Zhang, X.; Wang, H. Core-Shell Metallic Alloy Nanopillars-in-Dielectric Hybrid Metamaterials with Magneto-Plasmonic Coupling. *Mater. Today* **2021**, *51*, 39–47.
- (33) Zhang, B.; Kalaswad, M.; Rutherford, B. X.; Misra, S.; He, Z.; Wang, H.; Qi, Z.; Wissel, A. E.; Xu, X.; Wang, H. Au-Encapsulated Fe

- Nanorods in Oxide Matrix with Tunable Magneto-Optic Coupling Properties. ACS Appl. Mater. Interfaces 2020, 12 (46), 51827–51836.
- (34) Voyles, P. M.; Muller, D. A.; Grazul, J. L.; Citrin, P. H.; Gossmann, H.-J. L. Atomic-scale imaging of individual dopant atoms and clusters in highly n-type bulk Si. *Nature* **2002**, *416* (6883), 826–829.
- (35) Erni, R.; Heinrich, H.; Kostorz, G. Quantitative characterisation of chemical inhomogeneities in —Ag using high-resolution Z-contrast STEM. *Ultramicroscopy* **2003**, 94 (2), 125–133.
- (36) Klenov, D. O.; Stemmer, S. Contributions to the Contrast in Experimental High-Angle Annular Dark-Field Images. *Ultramicroscopy* **2006**, *106* (10), 889–901.
- (37) Misra, S.; Wang, H. Review on the Growth, Properties and Applications of Self-Assembled Oxide—Metal Vertically Aligned Nanocomposite Thin Films-Current and Future Perspectives. *Mater. Horiz.* **2021**, *8*, 869—884.
- (38) Cullity, B. D.; Graham, C. D. Introduction to Magnetic Materials; John Wiley & Sons, 2011.
- (39) Song, J.; Zhang, D.; Lu, P.; Wang, H.; Xu, X.; Meyerson, M. L.; Rosenberg, S. G.; Deitz, J.; Liu, J.; Wang, X.; Zhang, X.; et al. Anisotropic Optical and Magnetic Response in Self-Assembled TiN—CoFe2 Nanocomposites. *Mater. Today Nano* **2023**, 22, 100316.

### **□** Recommended by ACS

## Single-Domain Fe<sub>2</sub>CoAl Nanoparticles and Their Crystallite Size-Dependent Properties

Manisha Srivastava, Ananthakrishnan Srinivasan, et al.

MAY 22, 2023

THE JOURNAL OF PHYSICAL CHEMISTRY C

READ 🗹

### Synthesis and Characterization of Magnetoplasmonic Air-Stable Au@FeCo

Mary Sajini Devadas, Ellen Hondrogiannis, et al.

JANUARY 26, 2023

LANGMUIR

READ 🗹

## Magnetic Properties of High DC Bias Performance Fe-Si-B-C-Cr Amorphous Soft Magnetic Composites

Jibiao Shen, Guodong Wang, et al.

JULY 19, 2023

ACS APPLIED ELECTRONIC MATERIALS

READ 🗹

#### One-Pot Size-Controlled Synthesis of Tin- and Antimony-Based Intermetallic Nanoparticles

Andrew J. McGrath, Sergei A. Ivanov, et al.

DECEMBER 27, 2022

CHEMISTRY OF MATERIALS

READ 🗹

Get More Suggestions >